applied sciences

MDPI

Review

Dark-Field Hyperspectral Microscopy for Carbon Nanotubes Bioimaging

Ilnur Ishmukhametov and Rawil Fakhrullin *

Bionanotechnology Lab., Institute of Fundamental Medicine and Biology, Kazan Federal University, Kreml uramı 18, 420008 Kazan, Republic of Tatarstan, Russian Federation; irishmukhametov@gmail.com
* Correspondence: kazanbio@gmail.com

Abstract: Carbon nanotubes have emerged as a versatile and ubiquitous nanomaterial, finding applications in industry and biomedicine. As a result, biosafety concerns that stimulated the research focused on evaluation of carbon nanotube toxicity. In addition, biomedical applications of carbon nanotubes require their imaging and identification in biological specimens. Among other methods, dark-field microscopy has become a potent tool to visualise and identify carbon nanotubes in cells, tissues, and organisms. Based on the Tyndall effect, dark-field optical microscopy at higher magnification is capable of imaging nanoscale particles in live objects. If reinforced with spectral identification, this technology can be utilised for chemical identification and mapping of carbon nanotubes. In this article we overview the recent advances in dark-field/hyperspectral microscopy for the bioimaging of carbon nanotubes.

Keywords: optical dark-field microscopy; hyperspectral imaging; carbon nanotubes; biodistribution assessment

Citation: Ishmukhametov, I.; Fakhrullin, R. Dark-Field Hyperspectral Microscopy for Carbon Nanotubes Bioimaging. *Appl. Sci.* **2021**, *11*, 12132. https://doi.org/10.3390/app112412132

Academic Editor: Elzbieta Pach

Received: 1 November 2021
Accepted: 14 December 2021
Published: 20 December 2021

1. Introduction

Since their first discovery in 1991 [1], carbon nanotubes (CNTs) have gained much attention from the various fields of science [2–7] and industry [8–10] as a material with prominent physicochemical characteristics. Carbon nanotubes are the allotropic form of carbon, having a cylindrical hollow structure up to several tens of micrometres in length and, generally, up to tens of nanometres in diameter [11]. CNTs are formed by rolling up a graphene sheet, another allotropic form of carbon, consisting of hexagonally bonded atoms arranged in a honeycomb pattern. Nanotubes could be rolled up from either a single graphene sheet and thus named single-walled carbon nanotubes (SWCNTs) or multiple graphene sheets and hence named multi-walled carbon nanotubes (MWCNTs) [12]. The unique morphology and size of CNTs provide excellent mechanical properties, large specific surface area, high electrical and thermal conductivity, flexible surface chemistry and valuable optical properties [13]. These features have prompted CNTs to be applied as the key component in various composites, sensors, coatings, and devices [11,14]. Moreover, hollow-tube-shaped structures coupled with the possibility of functionalisation make them highly engaging in biomedical applications [15]. For example, CNTs can be applied as radio-imaging probes in positron emission tomography (PET) and single-photon emission computed tomography (SPECT) [16–18], contrast agents in magnetic resonance imaging (MRI) [19] and Raman spectroscopy [20]. Strong optical resonances in the near-infrared region also allow the use CNTs in near-infrared and photoacoustic imaging techniques [21–24]. Carbon nanotubes could also be adapted to modulate neuronal growth as biocompatible scaffolds controlling cell adhesion, differentiation and migration [25–27]. The distinctive shape of the nanomaterial favours building the biocompatible drug-delivery system for cancer or gene therapy [9]. However, despite where CNTs could be effectively applied, their extensive toxicity and biodistribution analyses are required [15]. It is undoubted that physicochemical properties significantly determine the toxicity of nanomaterials. In terms of nanotubes, the important

parameters, which form the fibre pathogenicity paradigm (FPP), are length, diameter, rigidity, and biopersistence [28]. The long and thin CNTs fulfil all FPP attributes and hence may possess highly inflammogenic and fibrogenic potential [29,30]. Among different techniques, such as particle size analysis, X-ray diffraction analysis (XRD), mass spectrometry, infrared spectroscopy, electrophoresis, cytotoxicity, and viability assays, primarily used to define nanoparticles' chemical structure, size distribution or toxicity, the microscopy techniques stand out as the versatile tool relevant to morphology characterisation and toxicity analysis [31–33].

Nowadays, three principal approaches to the microscopy of CNTs can be highlighted: electron microscopy, scanning probe microscopy (SPM), and optical microscopy. Electron-based imaging systems as well as SPM methods, such as transmission electron microscopy (TEM), scanning electron microscopy (SEM), atomic force microscopy (AFM) or scanning tunnelling microscopy (STM), are primarily used to define the ultrastructure of fabricated nanotubes and their mechanical properties, such as accurate dimensions, the number of layers, interlayer spacing, surface functionalisation, Young's modulus, adhesion, and stiffness [34]. However, they are not suitable for dynamic bioimaging studies of nanotubes since such visualisation is either labour- and time-consuming or requires special conditions, invasive sampling, and expensive equipment. On the other hand, conventional optical microscopy lacks these drawbacks. Nevertheless, optical imaging also could be challenging for tubes with several nanometres in diameter due to the diffraction barrier caused by the wave nature of light. Rayleigh's criterion may describe this limitation in resolution (R):

$$R = \frac{1.22 \times \lambda}{NA_{\text{objective}} + NA_{\text{condenser}}}, \quad (1)$$

where λ is the wavelength of light illuminated from a specimen, NA is the numerical aperture of the objective and the condenser. Thus, the theoretical limit for microscopy with visible light illumination does not overcome 180–250 nm. Therefore, various strategies and tools are utilised to directly detect nanomaterials in biological samples, including photothermal microscopy [35], surface plasmon resonance microscopy, and other recently developed super-resolution techniques [36]. However, established methods, such as fluorescence or dark-field microscopy (DFM), remain applicable in nanotoxicological studies due to simplicity, low cost, and the possibility of observing hundreds of samples [37–39]. At the same time, there is no review of the published studies conducting dark-field bioimaging of carbon nanotubes. Therefore, the scope of this mini-review is limited by the keywords: optical dark-field microscopy, carbon nanotubes, and biological studies. In the first section, we briefly introduce the background and fundamentals of dark-field microscopy. Then, we overview in vitro and in vivo studies of CNTs where DFM had been applied. Finally, we summarise our conclusions and provide an outlook on future prospects.

2. Dark-Field Microscopy

Dark-field microscopy is a scattering-based imaging technique where elastically scattered light from a specimen entering the objective forms the image, while incident light is blocked (Figure 1A). The fact that the light scattered from particles passes the objective leads to generating a clear and dark background with bright appearing objects, i.e., giving a higher signal-to-noise ratio (SNR) than in a conventional optical system [40]. In the case of nanosized objects, the scattering intensity may be approximated by the Rayleigh scattering theory, where the ratio of the refractive index of particles to the media is crucial to distinguish objects from the background [41]. Additionally, in noble metal nanoparticles, the prominent influence on the intensity provides a localised surface plasmon resonance (LSPR) effect, occurring when the electric field of incident light causes collective oscillations of electron density on the surface of particles [42]. Notably, the larger particles also scatter more intense light than the smaller ones [41,43]. Although carbon nanotubes could be directly observed through dark-field microscopy due to high aspect ratio [44] and Rayleigh scattering [45], deposition of nanoparticles with larger diameters or LSPR effect onto CNTs

is applied to visualise individual nanotubes (Figure 2A) [46,47] and produce enhanced scattering agents for cell imaging [48]. Besides endogenous factors of materials, the exogenous parameters, such as the medium of the sample, method of illumination, angle of incidence, and numerical aperture of the objective, also influence the resulting image. Thus, the CytoViva^{TM} enhanced dark-field illumination system (CytoViva, Auburn, Al, USA), widely used in biology and medicine, increases the SNR up to ten times by efficiently utilising these features [49,50]. In the enhanced dark-field microscopy (EDFM), the fibre optic illumination source is directly connected to the cardioid annular oil immersion dark-field condenser to reflect the aberration-free light at an oblique angle [51]. That type of condenser, in combination with high numerical aperture (NA) oil objectives, makes it possible to collect the scattered light of particles at wider angles, resolving nanoscale particles in biological samples [52,53].

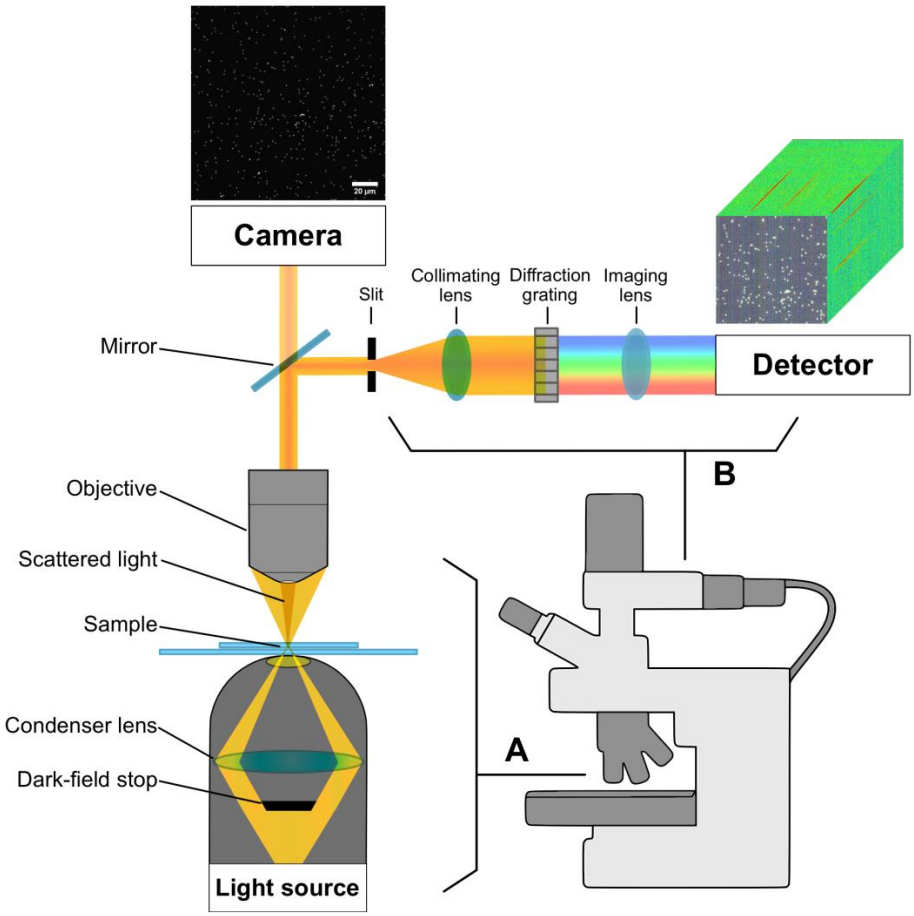

Figure 1. (**A**) Representative optical diagram of dark-field microscopy and (**B**) a scheme of spectral data cube acquisition on the example of 200 nm polystyrene nanoparticles.

Since the scattered spectrum of particles is highly affected by their physical, optical and electrical properties, dark-field microscopes may be equipped with hyperspectral sensors, thus obtaining spectral information with narrow bands at each pixel of an image (Figure 1B) [54]. Typically, the hyperspectral sensors used in biological studies acquired data of elastic scattering in the visible near-infrared range (VNIR; 400–1000 nm wavelength range), although there are setups with sensing in the short-wave infrared range (SWIR; 900–1700) or Raman scattering [55]. The hypercubes are captured from samples as three-dimensional data with two spatial dimensions (x, y) and one spectral (z). During the scan, the light from the specimen is almost entirely blocked, except the part that enters the narrow slit. Then, the collimated light is dispersed by a diffraction grating, and the detector captures its constitutive wavelengths. In the general scanning technique, called

"push broom", one spatial and spectral dimension is captured at a time. Thus, the process is performed line by line for the whole image. The resolving power (R_s) of the sensor is mainly determined by the diffraction grating and, similarly to the spatial resolution, could be described by Rayleigh's criterion:

$$R_s = \frac{\lambda}{\Delta\lambda}, \quad (2)$$

where $\Delta\lambda$ is the wavelength interval between two spectral lines resolved by the grating. Although in realistic conditions, the slit width and sensitivity of the camera also significantly influence the resulting spectral resolution, which, however, can still reach up to several nanometres [56]. EDFM coupled with hyperspectral imaging (HSI) allows for robust discrimination of nanoparticles within samples with subsequent identification based on their spectral characteristics (Figure 2C) [57]. For example, EDFM-HSI has been successfully used to measure the absorption capacity of CNTs (Figure 2B,D) [58] and identify nanotubes within living organisms [59].

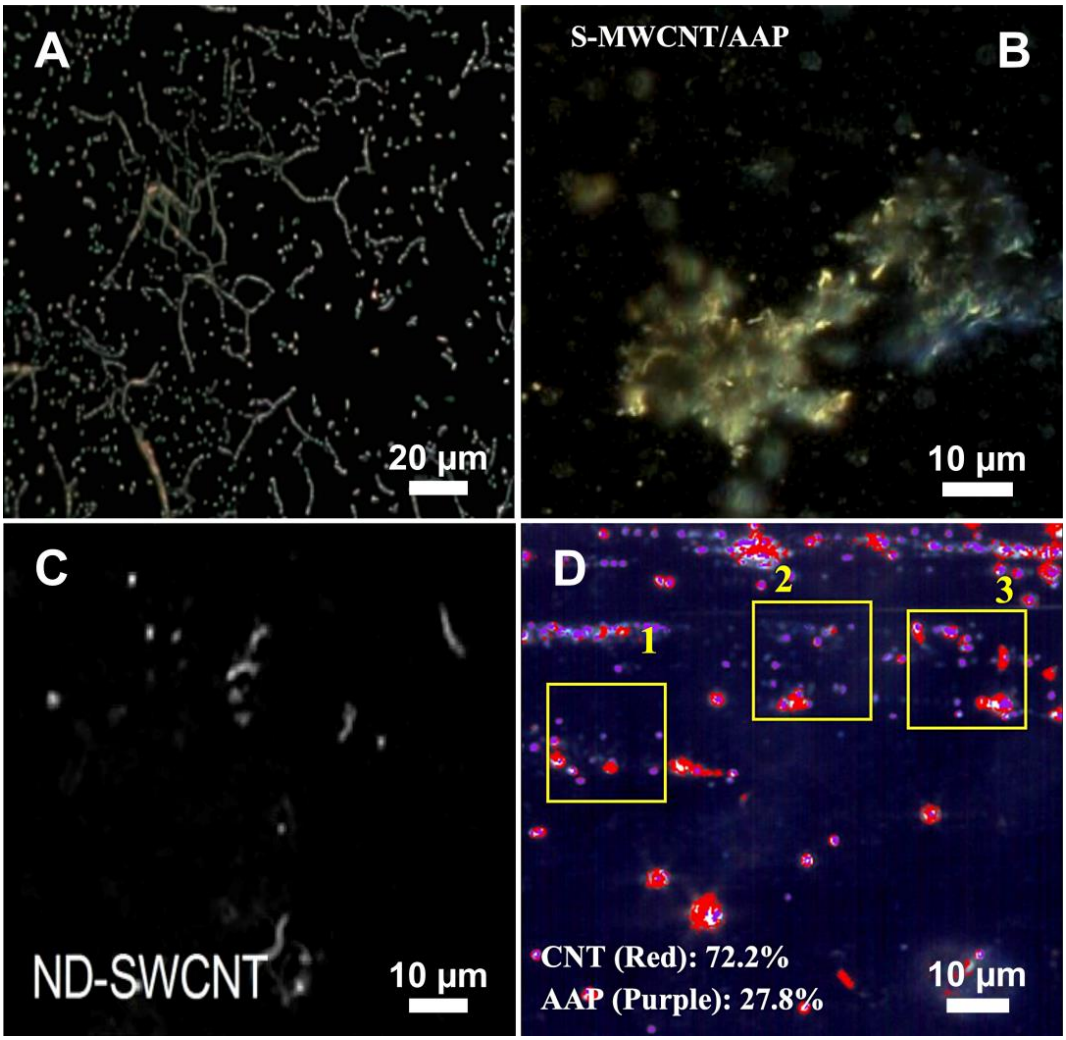

Figure 2. (**A**) Dark-field optical microscopy image of p-nitrobenzoic acid nanocrystals adsorb onto commercial dispersed CNTs. (**B**) Enhanced dark-field hyperspectral image of MWCNTs—acetaminophen (AAP) suspension. (**C**) Hyperspectral image of the Survanta®-dispersed SWCNTs suspension (0.1 mg/mL). (**D**) Hyperspectral imaging with spectrally identified MWCNTs as red pixels and AAP as purple pixels. Figure 2A adapted from Ref. [46] under the terms of the Creative Commons Attribution License (CC-BY 4.0). Figure 2C adapted from Ref. [57] under the terms of the Creative Commons Attribution License (CC-BY 2.0). Figure 2B,D adapted from Ref. [58]. Copyright 2021 American Chemical Society.

3. In Vitro Studies of CNTs

Dark-field microscopy is a versatile and easy-to-use tool for label-free, non-invasive observation of nanomaterials in vitro using model cell cultures. At the moment, DFM has been actively applied to visualise organic, inorganic and composite nanomaterials [60,61]. Carbon nanotubes possess a high aspect ratio and strong Rayleigh scattering, allowing for the detection of them in biological specimens. Table 1 summarises studies on mammalian cells treated with CNTs with the application of optical dark-field microscopy. Most of them involve the various CytoViva's enhanced dark-field microscopy setups since the unique illumination approach significantly increases signal-to-noise ratio resolving to observe even single nanotubes. For example, the synergistic effect of SWCNTs and etoposide on human pancreatic adenocarcinoma cells (PANC-1) viability were studied [62]. EDFM imaging demonstrated a time-dependent accumulation/distribution of SWCNTs in living cell samples, although it was hard to confirm CNT internalisation inside the cells. The same cell model was used in another study, where MWCNTs and polyethene glycol (PEG) composite was used for photothermal treatment of pancreatic cancer [63]. Using EDFM, dose-dependent internalisation of MWCNTs-PEG into PANC-1 cells after 1 h exposure was detected. An example of visualisation of single CNTs is reported in another toxicological study (Figure 3A) [64]. The murine macrophage cells (RAW 264.7) exposed with MWCNTs for different time points (2–48 h) were directly observed through EDFM, confirming the time-dependent accumulation of nanotubes onto the surface as well as inside the cells. While examining the influence of the biological environment on the dispersion of CNTs, the EDFM technique was applied to confirm the bioavailability of nanotube dispersions to immortalised bronchial epithelium cells (BEAS-2B cell line) [65].

The complications arising from identifying cellular compartments affected by CNTs could be overcome using correlative dark-field imaging of nanoparticles and fluorescence microscopy. Notably, this approach has been applied in a study focused on the repair mechanism of lung epithelial tissue in the presence of pollutants [66]. The CNT-treated human lung adenocarcinoma cells (A549 cell line) were used as the epithelial tissue model with inhaled particles to observe their influence on recovery kinetics. CytoViva dual-mode fluorescence-enhanced dark-field microscopy setup was used to obtain 3D-rendered images of cells stained with 4′,6-diamidino-2-phenylindole (DAPI) and rhodamine-phalloidin, which revealed strong attachment of CNTs to the cellular membrane and partial internalisation. The same technique was used in the study of proinflammatory and profibrotic activity of MWCNTs in A549 cells, macrophages (differentiated THP-1 cells) and fibroblasts (MRC-5; Figure 3C), that demonstrated comparatively higher uptake of CNTs in macrophages upon acute and prolonged exposure [67]. It is noted that increased uptake of nanotubes by macrophages could be due to their phagocytic activity and may cause fibrosis, which is also confirmed in the toxicogenomic analysis of macrophages treated with similar CNTs concentrations and exposure time [68]. Besides, a 3D rendering approach was applied to assess the internalisation of "long and thick" Mitsui-7 and "short and thin" Nanocyl-7000 MWCNTs on various cell types (bronchial and alveolar epithelial cells, mouse macrophages, and mesothelial cells) [69] as well as a complex organotypic model of alveolar tissue [70]. Nanocyl-7000 nanotubes appeared as densely packed aggregates in both cases, while Mitsui-7 were distinguishable as individual nanotubes. Nevertheless, the internalisation of both types of MWCNTs was observed in all cell models. Additionally, the cellular uptake of CNTs could be affected not only by dimensionality but also surface modification. Bai and colleagues investigated the influence of CNT functionalisation and protein corona formation on their biocompatibility [71]. It was discovered that carboxylation and base washing of MWCNTs increased cellular uptake. At the same time, coating nanotubes with bovine serum albumin (BSA) impacted cell absorption of only pristine nanotubes, which EDFM confirmed. Moreover, basic dye staining in a series of studies assessing the carcinogenic potential of pristine and surface functionalised CNTs on human small airway epithelial cells (SAECs) was applied to enhance cell contrast in EDFM [72–74]. Dark-field microscopy confirmed that carbon nanotubes either co-localised in the cytoplasm of cells

or punctured the cellular or nuclear membranes. Another study based on fluorescence and dark-field imaging showed that ovalbumin (OVA) could be successfully delivered into macrophages in the complex with CNTs [75]. Siegrist et al. investigated the genotoxicity of raw, heat-treated (HT) and nitrogen-doped (ND) carbon nanotubes on BEAS-2B and SAECs [76]. Utilising fluorescence-enhanced dark-field imaging, they were able to quantitatively assess the nuclear uptake of the individual nanotubes, which revealed consistently higher partitioning of raw MWCNTs in nuclei of BEAS-2B cells (Figure 3B). Additionally, simultaneous incubation of cells with high doses of CNTs and gold nanoparticles (AuNP) demonstrated aggregation of particles on cells which has not been observed in TEM images, pointing to the complementary role of the methods in distribution studies [77].

Apart from direct observations, distinctive spectral features of carbon nanotubes allow for mapping them in cell samples via hyperspectral imaging. One study showed that pre-treatment of SAECs with CNTs significantly enhances viral infectivity [78]. HSI mapping successfully detected SWCNTs and pandemic influenza A H1N1 virus (IAV) in cell samples as well as changes in their distribution patterns during co-exposure, suggesting the presence of nanotubes may influence IAV behaviour (Figure 3D). In the comparative cytotoxicity analysis of clay and graphene-based nanomaterials, the hyperspectral imaging technique allowed the identification of nanoparticles in vital and paraformaldehyde (PFA) fixed A549 cells correctly [79]. It was found that graphene oxide nanosheets and MWCNTs are penetrating cells less than nanoclays at the same concentration. HSI alongside fluorescence microscopy was also used to visualise the uptake and fate of SWCNTs and MWCNTs in a study of the fibrogenic effect of carbon nanotubes on human lung fibroblasts (CRL-1490) [80].

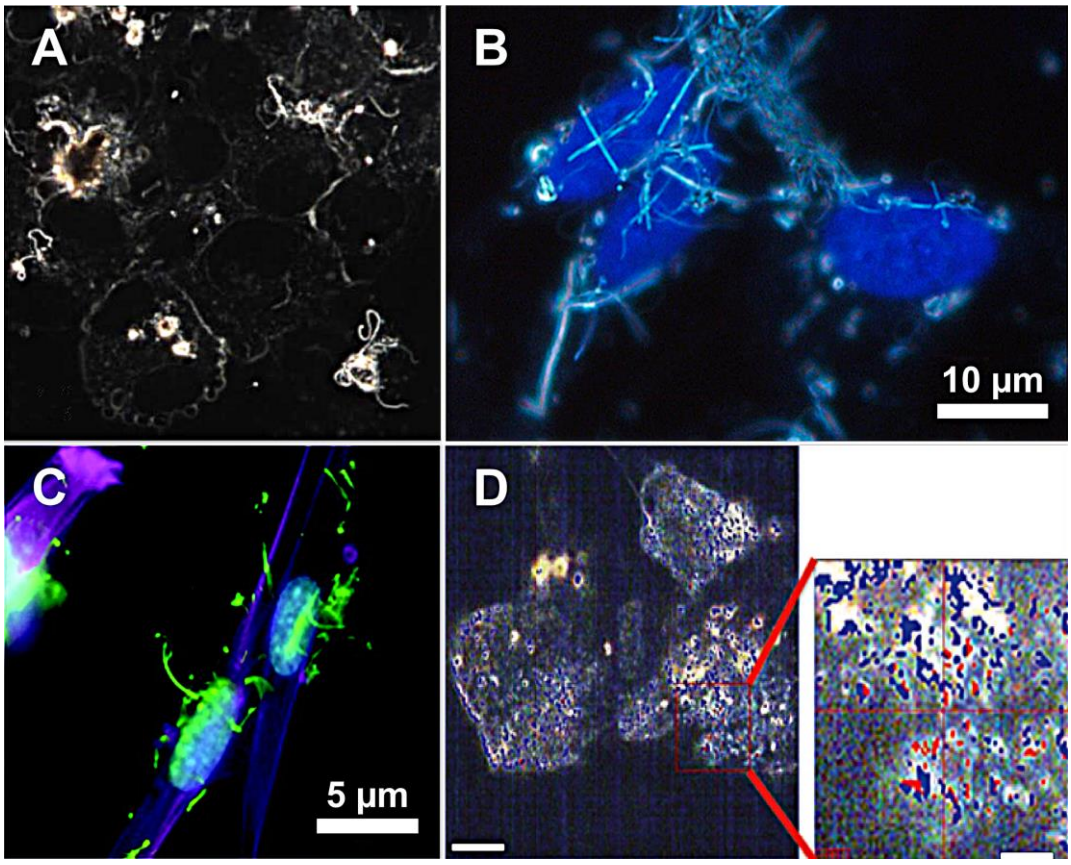

Figure 3. (**A**) Dark-field image of RAW 264.7 macrophages exposed to MWCNTs (0.2 µg/cm^2) for 24 h. (**B**) Composite image of enhanced dark-field showing the MWCNT fibres in the white and blue fluorescent DAPI stained nuclei of BEAS-2B cells after 24 h of exposure. (**C**) Fluorescence-enhanced dark-field microscopy images of MRC-5 cells exposed to 10 µg/mL of MWCNTs for 24 h. Magenta colour shows F-actin (cytoskeleton), blue colour represents DNA (cell nuclei), and green colour

shows MWCNTs. (**D**) Hyperspectral mapping of SAECs co-treated with SWCNTs (blue pixels) and pandemic H1N1 influenza A virus (red pixels). Figure 3A adapted from Ref. [64] under the terms of the Creative Commons Attribution License (CC-BY 3.0), scale not specified. Figure 3B adapted from Ref. [76] under the terms of the Creative Commons Attribution License (CC-BY 4.0). Figure 3C adapted from Ref. [67] under the terms of the Creative Commons Attribution License (CC-BY 4.0). Figure 3D adapted from Ref. [78] under the terms of the Creative Commons Attribution License (CC-BY 4.0), scale not specified.

Table 1. Overview of in vitro studies of carbon nanotubes applied dark-field imaging technique. L—length; D—diameter; W—width.

System	Cell Culture	Type of CNTs	Size of Tested CNTs	Treatment Condition	Sample Preparation	Results	Reference
CytoViva enhanced dark-field microscopy setup	PANC-1 cell line	SWCNTs	L: 0.3–3.0 μm, D: 0.7–1.6 nm	10 μg/mL for 1, 4, 8 and 24 h	Living cell samples	Imaging showed time-dependent cellular uptake/accumulation of SWCNTs started at 4 h of exposure	[62]
		MWCNTs-PEG	Hydrodynamic diameter is 298–728 nm	5, 10 and 50 μg/mL for 1 h	Not specified	EDFM demonstrated dose-dependent accumulation of CNTs in cells	[63]
	RAW 264.7 cell line	MWCNTs	L: >2 μm, D: 8–15 nm	0.2 μg/cm^2 for 2, 4, 6, 24 and 48 h	Living cell samples	Imaging revealed time-dependent accumulation of CNTs on the surface and inside the cells	[64]
	BEAS-2B cell line	TUBALL™ and HiPco SWCNTs	TUBALL™ (L: >5 μm, D: 1.6 ± 0.4 nm), HiPco (L: 0.1–1.0 μm, D: 0.8–1.2 nm)	2.5 μg/mL for 48 h	Living cell samples	Microscopy confirmed cell penetration of all types CNTs	[65]
CytoViva dual mode fluorescence-enhanced dark-field microscopy setup	A549 cell line	MWCNTs	L: ≈5.6 μm, W: 60 nm	5 and 10 μg/mL for 24 h	Fixed with PFA, stained with rhodamine-phalloidin and DAPI	Imaging confirmed both attachment to the cell membrane and partial internalisation of MWCNTs	[66]
	Macrophages, A549 and MRC-5 cell lines	MWCNTs	L: 5.66 ± 4.7 μm, D: 60.1 ± 18.2 nm	5 and 10 μg/mL for 24 and 96 h	Fixed with PFA, stained with rhodamine-phalloidin and DAPI	Microscopy demonstrated dose-dependent interaction of MWCNTs in all cell lines with increased association noted in THP-1 cells	[67]
	Organotypic model of human alveolar tissue MatTek EpiAlveolar, cocultured with (+) or without (-) MDMs	Mitsui-7 (long and thick) and Nanocyl-7000 (short and thin) MWCNTs	Not specified	≈0.9 and ≈2 μg/cm^2 of Mitsui-7 or ≈1 μg/cm^2 of Nanocyl-7000 for 3 weeks of repeated exposure in liquid aerosol form	Fixed with PFA, stained with rhodamine-phalloidin and DAPI	Imaging confirmed the association of both types of CNTs with cells in EpiAlveolar tissue. Nanocyl-7000 could only be seen after the additional processing of samples	[69]
	A549, 16HBE14o-, MeT-5A and J774A.1 cell lines	Mitsui-7 and Nanocyl-7000 MWCNTs	Mitsui-7 (L: 5.6 ± 4.7 μm, D: 60 ± 19 nm), Nanocyl-7000 (L: 0.8 ± 0.5 μm, D: 11 ± 5 nm)	10 μg/mL for 24 h	Fixed with PFA, stained with rhodamine-phalloidin and DAPI	Both types of MWCNTs were detectable within all cell types. Nanocyl-7000 were densely packed in cellular vesicles	[70]
	Rat aortic endothelial cells and RAW264.7 cell line	Uncoated and BSA-coated pristine (MWCNTs), carboxylated (F-MWCNTs), and base-washed carboxylated (BW-F-MWCNTs) nanotubes	MWCNTs (L: 1205 ± 360 nm, D: 34 ± 9 nm) ,F-MWCNTs (L: 767 ± 527 nm, D: 35 ± 11 nm), BW-F-MWCNTs (L: 737 ± 457 nm, D 35 ± 7 nm)	50 μg/mL for 24 h in serum-free medium	Fixed with PFA and stained with DAPI	Microscopy confirmed the lack of the influence of the coating on uptake of all types of MWCNTs by cells: F-MWCNTs and BW-F-MWCNTs are greater internalised in cells than pristine tubes	[71]

Table 1. *Cont.*

CytoViva enhanced dark-field microscopy setup	SAECs	SWCNTs and MWCNTs	SWCNTs (L: 1.08 µm, W: 270 nm), MWCNTs (L: 5.1 µm, W: 78 nm)	0.1 µg/mL for 24 and 48 h	Fixed with NBF and stained with toluidine blue	Imaging showed that both types of CNTs were co-localized in the cytoplasm of cells or puncturing the cellular and nuclear membranes	[72]
		'As-prepared' (pMWCNT), carboxylated-(MW-COOH), and aminated-(MW-NHx) CNTs	pMWCNT (L: 1.51 ± 0.001 µm, W: 26.0 ± 5.4 nm), MW-COOH (L: 1.86 ± 0.16 µm, W: 26.5 ± 1.0 nm), MW-NHx (D: 1.50 ± 0.0078 µm, W: 21.6 ± 0.6 nm)	0.288 µg/mL for 24 h	Not specified	Imaging showed that all the MWCNT particles co-localized with either the cytoplasm or nucleus of the cells	[73]
		MWCNTs	L: 8.1 ± 5 µm, D: 8.2 nm	0.06 µg/cm^2 for 24 h	Fixed with NBF and stained with toluidine blue	Microscopy analysis confirmed co-localization of CNTs with the plasma membrane, cytoplasm, and nucleus	[74]
CytoViva dual mode fluorescence-enhanced dark-field microscopy setup	Bone-marrow-derived macrophages	Uncoated and OVA-coated carboxylated MWCNT-2 and MWCNT-30	MWCNT-2 (L: ≈500 nm, D: 26 ± 5 nm) MWCNT-30 (L: ≈500 nm, D: 18 ± 3 nm)	25 µg/mL for 6 h in serum-free medium	Fixed with PFA and stained with DAPI	Imaging confirmed delivery of OVA into cells by both types of MWCNTs	[75]
	BEAS-2B	MWCNTs, MWCNT-HT and MWCNT-ND	MWCNTs (L: 5 ± 4 µm, D: 49 ± 13 nm), MWCNT-HT (L: 5 ± 4 µm, D: 57 ± 24 nm in), MWCNT-ND (L: 2 ± 3 µm, D: 30 ± 23 nm)	0.024, 0.24, 2.4, and 24 µg/mL for 24 h	Fixed with 100% ice cold methanol and stained with DAPI	Imaging showed a dose-dependent increase in all types of MWCNTs within the cell nucleus with higher partitioning of raw MWCNTs	[76]
	A549 cell line and human skin fibroblasts	SWCNTs	Hydrodynamic size is 7–214 nm	0.1, 0.25, 0.5, and 1 mg/mL for 24 h with AuNP	Fixed with PFA and stained with DAPI	SWCNTs were seen as large aggregates on the cells in EDF images which was not observed in TEM analysis	[77]
CytoViva dual mode fluorescence-enhanced dark-field microscopy coupled with hyperspectral imaging	SAECs	SWCNTs	Hydrodynamic radius is 106–243 nm	50 µg/mL for 24 h followed by viral infection	Fixed with cold acetone and methanol solution	Mapping showed that SWCNTs in isolated exposure appeared as irregular extracellular aggregates on cells; the distribution pattern of both virus and CNTs have changed during co-exposure	[78]
	A549 cell line	MWCNTs	L: 414.3 ± 79.3 nm	100 µg/mL for 24 h	Living cell samples. Samples fixed with PFA and stained with DAPI	Microscopy coupled with spectral matching revealed co-localisation of CNTs on the cell membrane	[79]
	CRL-1490 cell line	SWCNTs and MWCNTs	SWCNTs (L: 1 µm, W: 0.27 µm, MWCNTs (L: 5.1 µm, W: 0.078 µm)	0.02 µg/cm^2 for 24 h	Fixed with formaldehyde, stained with phalloidin and DAPI	Fluorescence microscopy showed uptake of all types of CNTs, which was then confirmed by hyperspectral imaging	[80]
CytoViva enhanced dark-field microscopy combined with SERS	BEAS-2B and HepG2 cell lines	LW-MWCNTs, LN-MWCNTs and SN-MWCNTs	LW-MWCNTs (L: 10–30 µm, D: 20–30 nm), LN-MWCNTs (L: 10–30 µm, D: 8–15 nm), SN-MWCNTs (L: 0.5–2 µm, D: 8–15 nm)	1 µg/mL for 24 h	Living cell samples	Imaging showed the interaction of all types of MWCNTs with both cell lines. Subsequent SERS analysis confirmed internalisation only of SN-MWCNTs	[55]
ImageStreamX multispectral imaging flow cytometer	Adherent macrophages and HUVEC line	FITC-MWCNTs conjugates	L: 340 nm, D: 20–30 nm	0, 10, 20, and 50 µg/mL for 20 h at 37 °C or 2 h at 4 °C. The conditioned medium was then incubated with recipient cells for 48 h	Trypsinised and fixed with formaldehyde	Flow cytometry imaging with dark-field, bright-field and fluorescent channels confirmed the dose-dependent increase in CNTs-labelled cells. The method also confirmed the possibility of CNT-labelling of recipient cells from conditioned medium	[81]

In addition to Rayleigh scattering, CNTs also exhibit Raman spectra that can be used to detect cellular uptake behaviour in combination with dark-field microscopy. The surface-enhanced Raman scattering (SERS) coupled with EDFM was used when investigating the effect of size and aspect ratio parameters of hydroxylated nanotubes on biocompatibility, which attested the intracellular uptake only of "short and narrow" (SN) rather than "long and narrow" (LN) or "long and wide" (LW) CNTs [55]. Besides dark-field microscopy, intercellular carbon nanotube translocations could also be assessed using flow cytometry imaging of single cells on bright-field, dark-field, and fluorescent channels simultaneously [81]. Interestingly, the fluorescence signal of CNTs-loaded cells was less reliable than light absorbance and scattering data obtained from bright-field and dark-field images.

4. In Vivo Studies of CNTs

Dark-field microscopy is widely used to observe the distribution of CNTs in tissues and cells following in vivo exposure on animals. Table 2 summarises applications of DFM on animal tissue and cell extracts. Generally, for the microscopic examination of tissue samples, the examined organs are fixed with neutral buffered formalin (NBF), paraffin-embedded, sectioned, stained with histological dyes after sacrification at specified post-exposure time points. The staining of sections enhances the contrast between CNTs and the tissue, which is hard to distinguish due to low brightness. Notably, each study under investigation has applied CytoViva's enhanced dark-field imaging technique, increasing resolution compared to traditional DFM. For instance, Sager et al. studied double-walled carbon nanotubes (DWCNTs) pulmonary bioactivity in the C57BL/6 mouse model [82]. The particles appeared as bright tubular inclusions on the tissue processed from mice dosed with CNTs via pharyngeal aspiration 56 days post-exposure. The same features were also noted in tissue and cell samples of the other in vivo studies [83–86]. Another study investigating the effect of surface carboxylation on CNT bioactivity showed that clearance of functionalised nanotubes from lungs occurred better than that of unmodified [87].

Similarly, the influence of carboxylation degree on CNT deposition in lungs of albino BALB/c mice was assessed by EDFM supplemented with hyperspectral imaging [88,89]. However, the often-used Spectral Angle Mapper algorithm, detecting particles within biological specimens by comparing their spectra with the endmember spectrum, could not recognise CNTs in the samples due to the similarity of their spectrum to that of the background of stained tissue. Therefore, the Spectral Feature Fitting was applied, which compares sample spectra with the brightest spectrum of CNTs in tissues. The method showed that highly functionalised MWCNTs had a higher lung burden and were more dispersed (Figure 4A). They also appeared to associate more with epithelial cells rather than alveolar macrophages, as occurs with pristine and less functionalised nanotubes. In order to avoid potential artefacts caused by instillation/agglomeration of CNTs because of a high single dose of particles, inhalation studies that closely mimic environmental conditions are performed. For example, Kim with colleagues have observed the toxicity of MWCNTs on Sprague Dawley (SD) rats after 5-day inhalation [90]. EDFM-HSI showed that nanotubes deposited in alveolar epithelium and macrophages persisted after 30 days post-exposure. The research group have pursued a study with extended exposure and postexposure times, finding that CNTs persist in the lungs after 90 days of the post-exposure period [91]. Another example of successful hyperspectral analysis is represented by the study of Smith et al., where it was applied to detect SWCNT uptake into circulating cells of severe combined immunodeficient (SCID) mice [92]. EDFM-HSI provided a map of the subcellular spatial distribution of nanomaterial, suggesting internalisation rather than binding to the membrane.

Table 2. Overview of in vivo studies of carbon nanotubes applied dark-field imaging technique. L—length; D—diameter; W—width.

System	Animal Model	Type of CNTs	Size of Tested CNTs	Treatment Condition	Sample Preparation	Results	Reference
CytoViva enhanced dark-field microscopy	C57BL/6J male mouse	DWCNTs	L: <5 μm, D: 1–2 nm	0, 1, 10, and 40 μg/mouse by pharyngeal aspiration 1-, 7- and 56-days post-exposure	Lungs were fixed with NBF, embedded, sectioned, and stained with Sirius Red	Microscopy revealed that CNTs generally observed within the interstitial tissue but also in condensed areas of alveolar macrophages	[82]
	C57BL/6N female mouse	NM-401 and NRCWE-006 MWCNTs	NM-401 (L: 4.0 ± 0.37 μm, D: 67 ± 24 nm), NRCWE-006 (L: 5.7 ± 0.49 μm, D: 29–173 nm)	54 μg/mouse by intratracheal instillation 1-year post-exposure	Lung and liver were fixed with formalin, embedded, sectioned, stained with haematoxylin and eosin	Imaging demonstrated the presence of single fibres both in lung and liver	[83]
	B6C3F1 male mice	MWCNTs	L: 4.46 μm, W: 58.5 nm	40 μg/mouse by pharyngeal aspiration 1-, 7-, and 28-days post-exposure	Lungs were fixed, embedded, sectioned, and stained with Picrosirius red and haematoxylin	Microscopy confirmed the appearance of CNTs in sections of mouse lung at 28 days post-exposure	[84]
	C57BL/6J male mouse	MWCNTs	L: 2–15 μm, D: 8–15 nm	20, 40 and 80 μg/mouse by pharyngeal aspiration 1-, 7-, 28-, and 56-days post-exposure	Precipitated cells from bronchoalveolar lavage fluid were stained with Romanovsky–Giemsa	Microscopy confirmed inclusions of CNTs in the cells after 56 days of exposure	[85]
		MWCNTs	The aerodynamic diameter is 1.3 μm	10 mg/m^3 for 2, 4, 8, and 12 days (5 h/day) by inhalation 1-day post-exposure	Lungs were fixed in 10% NBF, sectioned and stained with haematoxylin and eosin. The cells were isolated from whole lung lavage fluid	Imaging showed cell nucleus and pleural penetration by CNTs	[86]
		Bare (B) and carboxylated (F) MWCNTs	BMWCNTs (D: 42 nm), FMWCNTs (D: 44 nm). The length was not measured	40 μg/mouse by pharyngeal aspiration 56 days post-exposure	Lungs were fixed with NBF, embedded, sectioned, and stained with Sirius Red	Imaging demonstrated a greater amount of BMWCNTs within lungs in comparison with FMWCNTs	[87]
CytoViva enhanced dark-field microscopy coupled with hyperspectral imaging	BALB/c male mouse	Raw, minimally, and maximally carboxylated (f-) MWCNTs	MWCNTs (L: 10–30 μm), f-MWCNTs (L: 2.2 or 3.4 μm)	50 μg/25 g mouse by pharyngeal aspiration 7- and 28-days post-exposure	Lungs were fixed with PFA, embedded, sectioned, and stained with haematoxylin and eosin	Microscopy coupled with hyperspectral imaging analysis confirmed that the degree of carboxylation affected the lung burden	[88]
		Raw and carboxylated (f-) MWCNTs with different microwave radiation times (5–120 min)	MWCNTs (L: 10–30 μm, D: 20–30 nm). The hydrodynamic size of all MWCNT variants was in the range of 42–396 nm	1 mg/mL by intratracheal instillation 3 days post-exposure	Not specified	Microscopy coupled with hyperspectral image showed that degree of functionalisation is critical to the distribution and the number of deposited CNTs on the epithelial cells	[89]
	SD male rat	MWCNTs	L: 0.5–20 μm, D: 10–15 nm	0.16 ± 0.01, 0.34 ± 0.02 and 0.94 ± 0.02 mg/m^3 for 5 days by inhalation (6 h/day) 0- and 30-days post-exposure	Lungs fixed with NBF, embedded, sectioned, and stained with haematoxylin and eosin	EDFM-HSI showed that CNTs were deposited in the alveolar epithelium and the alveolar macrophages and persisted after 30 days of post-exposure	[90]
	Fischer 344 rat, male and female	MWCNTs	L: 0.5–20 μm, D: 10–15 nm	0.2, 0.5 and 1.0 mg/m^3 for 28 days by inhalation (6 h/day) 0-, 28- and 90-days post-exposure	Lungs fixed with NBF, embedded, sectioned, and stained with haematoxylin and eosin	Imaging coupled with spectral matching revealed persistence of CNTs even at 90 days of post-exposure; aggregated CNTs were observed at 28 days of post-exposure but resolved at 90 days	[91]
	SCID male mouse with tumour inoculation	Peptide- and dye-conjugated SWCNTs	L: 100–300, D: 0.8–1.2 nm	0.068 mg/mL (180 μL) by intravenous injection 2- and 6-h post-exposure	CNTs-laden living cells were isolated from blood using FACS	Microscopy with hyperspectral image analysis showed uptake of CNTs by circulating cells and subcellular distribution of nanotubes	[92]

Table 2. *Cont.*

System	Animal Model	Type of CNTs	Size of Tested CNTs	Treatment Condition	Sample Preparation	Results	Reference
CytoViva enhanced dark-field microscopy	C57BL/6J male mouse	MWCNTs	L: 3.86 μm, D: 49 ± 13.4 nm	10, 20, 40 and 80 μg/mouse by pharyngeal aspiration 1-, 7-, 28- and 56-days post-exposure	Lungs were fixed with NBF, embedded, sectioned, and stained with Sirius Red and haematoxylin	Imaging demonstrated that CNTs readily penetrate all cell membranes/boundaries of the lungs; the majority of the MWCNTs were found within or penetrating alveolar macrophages but rarely observed in the airways by the 7th day after postexposure	[93]
		MWCNTs	L: 4.3 μm	5 mg/m^3 for 12 days (5 h/day) by inhalation 1, 14, 28-, 84-, 168- and 336-days post-exposure	Tissue blocks (lung) were fixed, embedded, sectioned, and stained with Sirius Red and Mayer's haematoxylin	Microscopy analysis confirmed a decrease in MWCNTs lung burden from 28 to 18 μg during 336 days of post-exposure; the presence of singular nanotubes was unchanged over 168 days post-exposure, while the concentration of aggregated particles decreased	[94]
	SD male rat	MWCNTs	L: 3.9 μm, W: 49 nm	5 mg/m^3 for 1, 3 and 4 days (5 h/day) by inhalation 24 h post-exposure	Tissue blocks (lung, heart, kidney, and liver) were fixed, embedded, sectioned, and stained with Sirius Red and Mayer's haematoxylin	Imaging confirmed small translocation of CNTs from the lung to the extrapulmonary organs	[95]
	C57BL/6J male mouse	MWCNTs	L: 4.3 μm	5 mg/m^3 for 12 days (5 h/day) by inhalation 1- and 336-days post-exposure	Tissue blocks (lung, tracheobronchial lymph nodes, diaphragm, heart, kidney, liver, and brain) were fixed, embedded, sectioned, and stained with Sirius Red and Mayer's haematoxylin	Microscopy confirmed that inhaled MWCNTs are translocated from the lung to the extrapulmonary organs and accumulated with time	[96]
	WT and Scgb1a1-hSPLUNC1 TG mice	Chemically cut SWCNTs	L: ≈200 nm	80 μg/mouse by pharyngeal aspiration 7 days post-exposure	Not specified	Microscopy revealed a higher concentration of CNTs in WT mice with the predominance in the alveolar tissue region	[97]
	NADPH-oxidase-deficient and C57BL/6 mice	Oxidised SWCNTs	L: 0.4–2.4 μm	40 μg/mouse by pharyngeal aspiration 7- and 28-days post-exposure	Lungs were fixed, embedded, sectioned, stained with haematoxylin and eosin.	Microscopy confirmed the significant decrease in CNTs-laden macrophages by 28th-day post-exposure; the clearance of CNTs in NADPH-oxidase-deficient mouse was less effective compared to the control group	[98]

Despite some difficulties raised in recognising the particles using HSI in histologically processed samples, enhanced dark-field microscopy itself provides the possibility to quantitively assess the distribution of CNTs in tissues by standard morphometric grid point counting methods. Mercer et al. have implemented this technique to measure the lung burden distribution of CNTs, determining that the majority of nanotubes (68%) are within or penetrating alveolar macrophages [93]. In a later study, the research group managed to analyse changes in the distribution of MWCNTs in the lungs over 336 days post-exposure and the clearance rate of aggregated and singular particles (Figure 4B) [94]. The same approach with murine histology samples from extrapulmonary organs confirmed translocation and accumulation of CNTs in other tissues with time (Figure 4C) [95,96]. In addition, it was found that total CNT content in the lungs of transgenic mice overexpressing SPLUNC1 (Scgb1a1-hSPLUNC1 TG), a protein involved in the innate immune system response in the respiratory tract region, was lower than in their wild-type (WT) littermates [97]. Moreover, the clearance rate of oxidised CNTs by macrophages in NADPH-oxidase-deficient mice measured using the point-counting technique was also decreased compared to the control group [98].

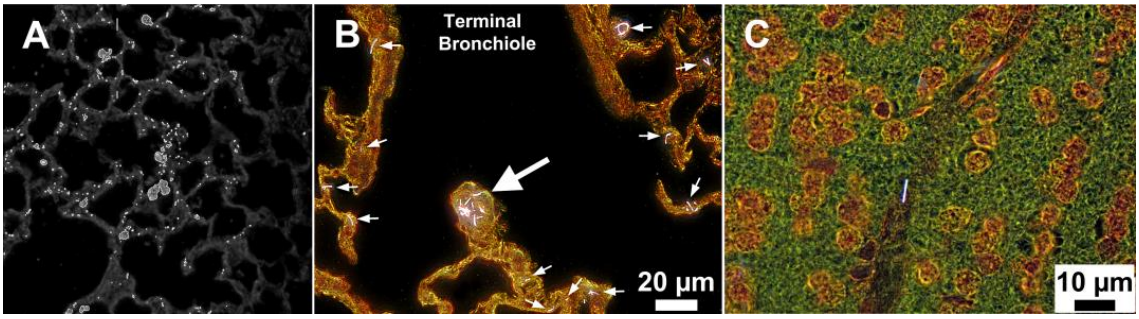

Figure 4. (**A**) Dark-field image (400×) using Particle Fitting Function to locate maximally carboxylated MWCNT in lung tissue of a BALB/c mouse following three-day particle exposure. Bright grey areas designate regions with nanotubes. (**B**) Enhanced dark-field image of the transition region between a terminal bronchiole and first alveolar duct bifurcation of C57BL/6J mouse at 168 days after exposure to MWCNT. The large arrow indicates a cluster of MWCNTs (white fibres) in the ridge of the first alveolar duct bifurcation. Smaller arrows indicate some of the numerous singlets and small MWCNT structures distributed throughout the alveolar septa of this critical transition region between conducting airways and gas exchange regions of the lungs. (**C**) Enhanced dark-field image of MWCNT fibres in the brain of C57BL/6J mouse at 336 days after inhalation exposure. MWCNT fibre is bright white, cell nuclei are brownish red, and other tissue elements are green. Figure 4A adapted from Ref. [89] under the terms of the Creative Commons Attribution License (CC-BY 4.0), scale not specified. Figure 4B adapted from Ref. [94] under the terms of the Creative Commons Attribution License (CC-BY 2.0). Figure 4C adapted from Ref. [96] under the terms of the Creative Commons Attribution License (CC-BY 2.0).

5. Conclusions and Future Prospects

Although dark-field imaging, as presented in the literature, allows direct observations of carbon nanotubes, the technique per se is insufficient for cell-nanoparticle identification. Modifications of DFM, such as enhanced dark-field optics coupled with fluorescence modules and hyperspectral sensors, have significantly increased the applicability of the method for cell biology, permitting spectral identification of particles, quantitative and qualitative analysis of cellular and nuclear uptake, and assessment of drug delivery efficiency. Comprehensive in vivo distribution studies of carbon nanotubes have demonstrated benefits from the EDFM-his technique over conventional methods due to fast sampling and robust detection in tissue sections. However, the method is not without the limitations arising when accurate subcellular imaging is needed. The hyperspectral analysis is also complicated in the case of histological staining, leading to the possibility of a false-positive outcome. At the same time, the increase in the amount of heterogenous spatio-spectral information obtained using correlation microscopy, as well as its still-developing stage,

leads to another challenge of efficient data processing. Recent studies have shown the power of machine learning algorithms, including neural networks in environmental studies and bacterial identification. This approach automates spectral feature selection, excluding the necessity for data pre-processing, and may help improve the performance of EDFM-HSI for nanomaterial systematic investigation in the future.

Author Contributions: Writing—original draft preparation, I.I.; writing—review and editing, R.F. All authors have read and agreed to the published version of the manuscript.

Funding: The work was funded by Russian Science Foundation grant 20-13-00247.

Institutional Review Board Statement: Not applicable.

Informed Consent Statement: Not applicable.

Conflicts of Interest: The authors declare no conflict of interest.

References

1. Iijima, S. Helical microtubules of graphitic carbon. *Nature* **1991**, *354*, 56–58. [CrossRef]
2. Trojanowicz, M. Analytical applications of carbon nanotubes: A review. *TrAC Trends Anal. Chem.* **2006**, *25*, 480–489. [CrossRef]
3. Saliev, T. The Advances in Biomedical Applications of Carbon Nanotubes. *C* **2019**, *5*, 29. [CrossRef]
4. Lan, Y.; Wang, Y.; Ren, Z.F. Physics and applications of aligned carbon nanotubes. *Adv. Phys.* **2011**, *60*, 553–678. [CrossRef]
5. Bekyarova, E.; Ni, Y.; Malarkey, E.B.; Montana, V.; McWilliams, J.L.; Haddon, R.C.; Parpura, V. Applications of Carbon Nanotubes in Biotechnology and Biomedicine. *J. Biomed. Nanotechnol.* **2005**, *1*, 3–17. [CrossRef]
6. Schnorr, J.M.; Swager, T.M. Emerging Applications of Carbon Nanotubes. *Chem. Mater.* **2011**, *23*, 646–657. [CrossRef]
7. Jain, N.; Gupta, E.; Kanu, N.J. Plethora of Carbon Nanotubes Applications in Various Fields–A State-of-the-Art-Review. *Smart Sci.* **2021**, 1–24. [CrossRef]
8. Cai, L.; Wang, C. Carbon Nanotube Flexible and Stretchable Electronics. *Nanoscale Res. Lett.* **2015**, *10*, 320. [CrossRef]
9. He, H.; Pham-Huy, L.A.; Dramou, P.; Xiao, D.; Zuo, P.; Pham-Huy, C. Carbon Nanotubes: Applications in Pharmacy and Medicine. *Biomed Res. Int.* **2013**, *2013*, 1–12. [CrossRef] [PubMed]
10. Kausar, A.; Rafique, I.; Muhammad, B. Review of Applications of Polymer/Carbon Nanotubes and Epoxy/CNT Composites. *Polym. Plast. Technol. Eng.* **2016**, *55*, 1167–1191. [CrossRef]
11. Nasir, S.; Hussein, M.; Zainal, Z.; Yusof, N. Carbon-Based Nanomaterials/Allotropes: A Glimpse of Their Synthesis, Properties and Some Applications. *Materials* **2018**, *11*, 295. [CrossRef]
12. Aqel, A.; El-Nour, K.M.M.A.; Ammar, R.A.A.; Al-Warthan, A. Carbon nanotubes, science and technology part (I) structure, synthesis and characterisation. *Arab. J. Chem.* **2012**, *5*, 1–23. [CrossRef]
13. Eatemadi, A.; Daraee, H.; Karimkhanloo, H.; Kouhi, M.; Zarghami, N.; Akbarzadeh, A.; Abasi, M.; Hanifehpour, Y.; Joo, S.W. Carbon nanotubes: Properties, synthesis, purification, and medical applications. *Nanoscale Res. Lett.* **2014**, *9*, 393. [CrossRef]
14. Ramirez-de-Arellano, J.M.; Canales, M.; Magaña, L.F. Carbon Nanostructures Doped with Transition Metals for Pollutant Gas Adsorption Systems. *Molecules* **2021**, *26*, 5346. [CrossRef]
15. Zhang, C.; Wu, L.; de Perrot, M.; Zhao, X. Carbon Nanotubes: A Summary of Beneficial and Dangerous Aspects of an Increasingly Popular Group of Nanomaterials. *Front. Oncol.* **2021**, *11*, 2908 . [CrossRef]
16. Yang, C.-T.; Ghosh, K.K.; Padmanabhan, P.; Langer, O.; Liu, J.; Eng, D.N.C.; Halldin, C.; Gulyás, B. PET-MR and SPECT-MR multimodality probes: Development and challenges. *Theranostics* **2018**, *8*, 6210–6232. [CrossRef] [PubMed]
17. Kazakov, A.G.; Garashchenko, B.L.; Ivanova, M.K.; Vinokurov, S.E.; Myasoedov, B.F. Carbon Nanomaterials for Sorption of 68Ga for Potential Using in Positron Emission Tomography. *Nanomaterials* **2020**, *10*, 1090. [CrossRef] [PubMed]
18. Negri, V.; Pacheco-Torres, J.; Calle, D.; López-Larrubia, P. Carbon Nanotubes in Biomedicine. In *Surface-Modified Nanobiomaterials for Electrochemical and Biomedicine Applications*; Puente-Santiago, A.R., Rodríguez-Padrón, D., Eds.; Springer International Publishing: New York, NY, USA, 2020; pp. 177–217. ISBN 978-3-030-55501-6.
19. Gong, H.; Peng, R.; Liu, Z. Carbon nanotubes for biomedical imaging: The recent advances. *Adv. Drug Deliv. Rev.* **2013**, *65*, 1951–1963. [CrossRef] [PubMed]
20. Zhang, Y.; Hong, H.; Cai, W. Imaging with Raman Spectroscopy. *Curr. Pharm. Biotechnol.* **2010**, *11*, 654–661. [CrossRef]
21. Godin, A.G.; Setaro, A.; Gandil, M.; Haag, R.; Adeli, M.; Reich, S.; Cognet, L. Photoswitchable single-walled carbon nanotubes for super-resolution microscopy in the near-infrared. *Sci. Adv.* **2019**, *5*. [CrossRef]
22. De La Zerda, A.; Zavaleta, C.; Keren, S.; Vaithilingam, S.; Bodapati, S.; Liu, Z.; Levi, J.; Smith, B.R.; Ma, T.-J.; Oralkan, O.; et al. Carbon nanotubes as photoacoustic molecular imaging agents in living mice. *Nat. Nanotechnol.* **2008**, *3*, 557–562. [CrossRef]
23. Yudasaka, M.; Yomogida, Y.; Zhang, M.; Tanaka, T.; Nakahara, M.; Kobayashi, N.; Okamatsu-Ogura, Y.; Machida, K.; Ishihara, K.; Saeki, K.; et al. Near-Infrared Photoluminescent Carbon Nanotubes for Imaging of Brown Fat. *Sci. Rep.* **2017**, *7*, 44760. [CrossRef]
24. Zhang, N.; Lu, C.; Chen, M.; Xu, X.; Shu, G.; Du, Y.; Ji, J. Recent advances in near-infrared II imaging technology for biological detection. *J. Nanobiotechnology* **2021**, *19*, 132. [CrossRef]

25. Lee, W.; Parpura, V. Carbon nanotubes as substrates/scaffolds for neural cell growth. In *Progress in Brain Research*; Elsevier: Amsterdam, The Netherlands, 2009; pp. 110–125. ISBN 978-0-444-53431-6.
26. Vicentini, N.; Gatti, T.; Salerno, M.; Hernandez Gomez, Y.S.; Bellon, M.; Gallio, S.; Marega, C.; Filippini, F.; Menna, E. Effect of different functionalized carbon nanostructures as fillers on the physical properties of biocompatible poly(l-lactic acid) composites. *Mater. Chem. Phys.* **2018**, *214*, 265–276. [CrossRef]
27. Lee, S.-J.; Zhu, W.; Nowicki, M.; Lee, G.; Heo, D.N.; Kim, J.; Zuo, Y.Y.; Zhang, L.G. 3D printing nano conductive multi-walled carbon nanotube scaffolds for nerve regeneration. *J. Neural Eng.* **2018**, *15*, 016018. [CrossRef] [PubMed]
28. Donaldson, K.; Murphy, F.A.; Duffin, R.; Poland, C.A. Asbestos, carbon nanotubes and the pleural mesothelium: A review and the hypothesis regarding the role of long fibre retention in the parietal pleura, inflammation and mesothelioma. *Part. Fibre Toxicol.* **2010**, *7*, 5. [CrossRef]
29. Boyles, M.S.P.; Young, L.; Brown, D.M.; MacCalman, L.; Cowie, H.; Moisala, A.; Smail, F.; Smith, P.J.W.; Proudfoot, L.; Windle, A.H.; et al. Multi-walled carbon nanotube induced frustrated phagocytosis, cytotoxicity and pro-inflammatory conditions in macrophages are length dependent and greater than that of asbestos. *Toxicol. Vitr.* **2015**, *29*, 1513–1528. [CrossRef]
30. Manke, A.; Luanpitpong, S.; Dong, C.; Wang, L.; He, X.; Battelli, L.; Derk, R.; Stueckle, T.; Porter, D.; Sager, T.; et al. Effect of Fiber Length on Carbon Nanotube-Induced Fibrogenesis. *Int. J. Mol. Sci.* **2014**, *15*, 7444–7461. [CrossRef]
31. Savage, D.T.; Hilt, J.Z.; Dziubla, T.D. In Vitro Methods for Assessing Nanoparticle Toxicity. In *Methods in Molecular Biology (Clifton, N.J.)*; Humana Press: New York, NY, USA, 2019; pp. 1–29. ISBN 978-1-4939-8916-4.
32. Kong, B.; Seog, J.H.; Graham, L.M.; Lee, S.B. Experimental considerations on the cytotoxicity of nanoparticles. *Nanomedicine* **2011**, *6*, 929–941. [CrossRef]
33. Drasler, B.; Sayre, P.; Steinhäuser, K.G.; Petri-Fink, A.; Rothen-Rutishauser, B. In vitro approaches to assess the hazard of nanomaterials. *NanoImpact* **2017**, *8*, 99–116. [CrossRef]
34. Mourdikoudis, S.; Pallares, R.M.; Thanh, N.T.K. Characterization techniques for nanoparticles: Comparison and complementarity upon studying nanoparticle properties. *Nanoscale* **2018**, *10*, 12871–12934. [CrossRef]
35. Adhikari, S.; Spaeth, P.; Kar, A.; Baaske, M.D.; Khatua, S.; Orrit, M. Photothermal Microscopy: Imaging the Optical Absorption of Single Nanoparticles and Single Molecules. *ACS Nano* **2020**, *14*, 16414–16445. [CrossRef] [PubMed]
36. Ghamsari, M.S. Introductory Chapter: Nano-bioimaging—Past, Present, and Future. In *State of the Art in Nano-Bioimaging*; InTech: London, UK, 2018; ISBN 978-1-78923-294-3.
37. Ostrowski, A.; Nordmeyer, D.; Boreham, A.; Holzhausen, C.; Mundhenk, L.; Graf, C.; Meinke, M.C.; Vogt, A.; Hadam, S.; Lademann, J.; et al. Overview about the localization of nanoparticles in tissue and cellular context by different imaging techniques. *Beilstein J. Nanotechnol.* **2015**, *6*, 263–280. [CrossRef]
38. Fakhrullin, R.; Nigamatzyanova, L.; Fakhrullina, G. Dark-field/hyperspectral microscopy for detecting nanoscale particles in environmental nanotoxicology research. *Sci. Total Environ.* **2021**, *772*, 145478. [CrossRef]
39. García-Rodríguez, A.; Rubio, L.; Vila, L.; Xamena, N.; Velázquez, A.; Marcos, R.; Hernández, A. The Comet Assay as a Tool to Detect the Genotoxic Potential of Nanomaterials. *Nanomaterials* **2019**, *9*, 1385. [CrossRef] [PubMed]
40. Tanaka, K.; Fujioka, Y.; Kubono, A.; Akiyama, R. Electrically developed morphology of carbon nanoparticles in suspensions monitored by in situ optical observations under sinusoidal electric field. *Colloid Polym. Sci.* **2006**, *284*, 562–567. [CrossRef]
41. Truong, P.L.; Ma, X.; Sim, S.J. Resonant Rayleigh light scattering of single Au nanoparticles with different sizes and shapes. *Nanoscale* **2014**, *6*, 2307. [CrossRef]
42. Fong, K.E.; Yung, L.-Y.L. Localized surface plasmon resonance: A unique property of plasmonic nanoparticles for nucleic acid detection. *Nanoscale* **2013**, *5*, 12043. [CrossRef]
43. Weigel, A.; Sebesta, A.; Kukura, P. Dark Field Microspectroscopy with Single Molecule Fluorescence Sensitivity. *ACS Photonics* **2014**, *1*, 848–856. [CrossRef]
44. Gaillard, J.; Skove, M.; Rao, A.M. Mechanical properties of chemical vapor deposition-grown multiwalled carbon nanotubes. *Appl. Phys. Lett.* **2005**, *86*, 1–3. [CrossRef]
45. Mishra, A.; Clayton, K.; Velasco, V.; Williams, S.J.; Wereley, S.T. Dynamic optoelectric trapping and deposition of multiwalled carbon nanotubes. *Microsystems Nanoeng.* **2016**, *2*, 16005. [CrossRef] [PubMed]
46. Zeevi, G.; Shlafman, M.; Tabachnik, T.; Rogachevsky, Z.; Rechnitz, S.; Goldshtein, I.; Shlafman, S.; Gordon, N.; Alchanati, G.; Itzhak, M.; et al. Automated circuit fabrication and direct characterization of carbon nanotube vibrations. *Nat. Commun.* **2016**, *7*, 12153. [CrossRef] [PubMed]
47. Zhang, R.; Zhang, Y.; Zhang, Q.; Xie, H.; Wang, H.; Nie, J.; Wen, Q.; Wei, F. Optical visualization of individual ultralong carbon nanotubes by chemical vapour deposition of titanium dioxide nanoparticles. *Nat. Commun.* **2013**, *4*, 1–7. [CrossRef] [PubMed]
48. Zhang, L.; Zhen, S.J.; Sang, Y.; Li, J.Y.; Wang, Y.; Zhan, L.; Peng, L.; Wang, J.; Li, Y.F.; Huang, C.Z. Controllable preparation of metal nanoparticle/carbon nanotube hybrids as efficient dark field light scattering agents for cell imaging. *Chem. Commun.* **2010**, *46*, 4303–4305. [CrossRef]
49. Zamora-Perez, P.; Tsoutsi, D.; Xu, R.; Rivera_Gil, P. Hyperspectral-Enhanced Dark Field Microscopy for Single and Collective Nanoparticle Characterization in Biological Environments. *Materials* **2018**, *11*, 243. [CrossRef] [PubMed]
50. Lawrence, S. Enhanced Darkfield Optical Microscopy Opens New Nano-Scale Imaging Possibilities. *Micros. Today* **2021**, *29*, 50–55. [CrossRef]

51. Sanderson, J. Condensers and Eyepieces. In *Understanding Light Microscopy*; John Wiley & Sons, Ltd.: Chichester, UK, 2019; pp. 161–175. ISBN 9780470973752.
52. Gorbachevskii, M.V.; Stavitskaya, A.V.; Novikov, A.A.; Fakhrullin, R.F.; Rozhina, E.V.; Naumenko, E.A.; Vinokurov, V.A. Fluorescent gold nanoclusters stabilized on halloysite nanotubes: In vitro study on cytotoxicity. *Appl. Clay Sci.* **2021**, *207*, 106106. [CrossRef]
53. Austin, C.A.; Hinkley, G.K.; Mishra, A.R.; Zhang, Q.; Umbreit, T.H.; Betz, M.W.; Wildt, B.E.; Casey, B.J.; Francke-Carroll, S.; Hussain, S.M.; et al. Distribution and accumulation of 10 nm silver nanoparticles in maternal tissues and visceral yolk sac of pregnant mice, and a potential effect on embryo growth. *Nanotoxicology* **2016**, *10*, 654–661. [CrossRef]
54. Roth, G.A.; Tahiliani, S.; Neu-Baker, N.M.; Brenner, S.A. Hyperspectral microscopy as an analytical tool for nanomaterials. *Wiley Interdiscip. Rev. Nanomed. Nanobiotechnol.* **2015**, *7*, 565–579. [CrossRef] [PubMed]
55. Chatterjee, N.; Yang, J.; Kim, S.; Joo, S.W.; Choi, J. Diameter size and aspect ratio as critical determinants of uptake, stress response, global metabolomics and epigenetic alterations in multi-wall carbon nanotubes. *Carbon N. Y.* **2016**, *108*, 529–540. [CrossRef]
56. Huebschman, M.L.; Schultz, R.A.; Garner, H.R. Characteristics and capabilities of the hyperspectral imaging microscope. *IEEE Eng. Med. Biol. Mag.* **2002**, *21*, 104–117. [CrossRef]
57. Wang, L.; Castranova, V.; Mishra, A.; Chen, B.; Mercer, R.R.; Schwegler-Berry, D.; Rojanasakul, Y. Dispersion of single-walled carbon nanotubes by a natural lung surfactant for pulmonary in vitro and in vivo toxicity studies. *Part. Fibre Toxicol.* **2010**, *7*, 31. [CrossRef]
58. Wang, Y.; Fu, W.; Shen, Y.; Badireddy, A.R.; Zhang, W.; Huang, H. Hyperspectral Imaging Microscopy of Acetaminophen Adsorbed on Multiwalled Carbon Nanotubes. *Langmuir* **2018**, *34*, 13210–13218. [CrossRef]
59. Schwab, F.; Bucheli, T.D.; Camenzuli, L.; Magrez, A.; Knauer, K.; Sigg, L.; Nowack, B. Diuron Sorbed to Carbon Nanotubes Exhibits Enhanced Toxicity to Chlorella vulgaris. *Environ. Sci. Technol.* **2013**, *47*, 7012–7019. [CrossRef]
60. Akhatova, F.; Danilushkina, A.; Kuku, G.; Saricam, M.; Culha, M.; Fakhrullin, R. Simultaneous Intracellular Detection of Plasmonic and Non-Plasmonic Nanoparticles Using Dark-Field Hyperspectral Microscopy. *Bull. Chem. Soc. Jpn.* **2018**, *91*, 1640–1645. [CrossRef]
61. Zamora-Perez, P.; Pelaz, B.; Tsoutsi, D.; Soliman, M.G.; Parak, W.J.; Rivera-Gil, P. Hyperspectral-enhanced dark field analysis of individual and collective photo-responsive gold–copper sulfide nanoparticles. *Nanoscale* **2021**, *13*, 13256–13272. [CrossRef] [PubMed]
62. Mahmood, M.; Xu, Y.; Dantuluri, V.; Mustafa, T.; Zhang, Y.; Karmakar, A.; Casciano, D.; Ali, S.; Biris, A. Carbon nanotubes enhance the internalization of drugs by cancer cells and decrease their chemoresistance to cytostatics. *Nanotechnology* **2013**, *24*. [CrossRef] [PubMed]
63. Mocan, T.; Matea, C.T.; Cojocaru, I.; Ilie, I.; Tabaran, F.A.; Zaharie, F.; Iancu, C.; Bartos, D.; Mocan, L. Photothermal treatment of human pancreatic cancer using PEGylated multi-walled carbon nanotubes induces apoptosis by triggering mitochondrial membrane depolarization mechanism. *J. Cancer* **2014**, *5*, 679–688. [CrossRef]
64. Khaliullin, T.O.; Fatkhutdinova, L.M.; Zalyalov, R.R.; Kisin, E.R.; Murray, A.R.; Shvedova, A.A. In vitro toxic effects of different types of carbon nanotubes. *IOP Conf. Ser. Mater. Sci. Eng.* **2015**, *98*, 012021. [CrossRef]
65. Timerbulatova, G.A.; Dimiev, A.M.; Khamidullin, T.L.; Boichuk, S.V.; Dunaev, P.D.; Fakhrullin, R.F.; Khaertdinov, N.N.; Porfiryeva, N.N.; Khaliullin, T.O.; Fatkhutdinova, L.M. Dispersion of Single-Walled Carbon Nanotubes in Biocompatible Environments. *Nanotechnologies Russ.* **2020**, *15*, 437–444. [CrossRef]
66. Septiadi, D.; Abdussalam, W.; Rodriguez-Lorenzo, L.; Spuch-Calvar, M.; Bourquin, J.; Petri-Fink, A.; Rothen-Rutishauser, B. Revealing the Role of Epithelial Mechanics and Macrophage Clearance during Pulmonary Epithelial Injury Recovery in the Presence of Carbon Nanotubes. *Adv. Mater.* **2018**, *30*, 1–9. [CrossRef] [PubMed]
67. Chortarea, S.; Zerimariam, F.; Barosova, H.; Septiadi, D.; Clift, M.J.D.; Petri-Fink, A.; Rothen-Rutishauser, B. Profibrotic Activity of Multiwalled Carbon Nanotubes Upon Prolonged Exposures in Different Human Lung Cell Types. *Appl. Vitr. Toxicol.* **2019**, *5*, 47–61. [CrossRef]
68. Saarimäki, L.A.; Kinaret, P.A.S.; Scala, G.; del Giudice, G.; Federico, A.; Serra, A.; Greco, D. Toxicogenomics analysis of dynamic dose-response in macrophages highlights molecular alterations relevant for multi-walled carbon nanotube-induced lung fibrosis. *NanoImpact* **2020**, *20*, 100274. [CrossRef]
69. Barosova, H.; Maione, A.G.; Septiadi, D.; Sharma, M.; Haeni, L.; Balog, S.; O'Connell, O.; Jackson, G.R.; Brown, D.; Clippinger, A.J.; et al. Use of EpiAlveolar Lung Model to Predict Fibrotic Potential of Multiwalled Carbon Nanotubes. *ACS Nano* **2020**, *14*, 3941–3956. [CrossRef]
70. Steinmetz, L.; Bourquin, J.; Barosova, H.; Haeni, L.; Caldwell, J.; Milosevic, A.; Geers, C.; Bonmarin, M.; Taladriz-Blanco, P.; Rothen-Rutishauser, B.; et al. Rapid and sensitive quantification of cell-associated multi-walled carbon nanotubes. *Nanoscale* **2020**, *12*, 17362–17372. [CrossRef]
71. Bai, W.; Wu, Z.; Mitra, S.; Brown, J.M. Effects of Multiwalled Carbon Nanotube Surface Modification and Purification on Bovine Serum Albumin Binding and Biological Responses. *J. Nanomater.* **2016**, *2016*, 2159537. [CrossRef]
72. Wang, L.; Stueckle, T.A.; Mishra, A.; Derk, R.; Meighan, T.; Castranova, V.; Rojanasakul, Y. Neoplastic-like transformation effect of single-walled and multi-walled carbon nanotubes compared to asbestos on human lung small airway epithelial cells. *Nanotoxicology* **2014**, *8*, 485–507. [CrossRef] [PubMed]

73. Stueckle, T.A.; Davidson, D.C.; Derk, R.; Wang, P.; Friend, S.; Schwegler-Berry, D.; Zheng, P.; Wu, N.; Castranova, V.; Rojanasakul, Y.; et al. Effect of surface functionalizations of multi-walled carbon nanotubes on neoplastic transformation potential in primary human lung epithelial cells. *Nanotoxicology* **2017**, *11*, 613–624. [CrossRef] [PubMed]
74. Stueckle, T.A.; Davidson, D.C.; Derk, R.; Kornberg, T.G.; Schwegler-Berry, D.; Pirela, S.V.; Deloid, G.; Demokritou, P.; Luanpitpong, S.; Rojanasakul, Y.; et al. Evaluation of tumorigenic potential of CeO2 and Fe2O3 engineered nanoparticles by a human cell in vitro screening model. *NanoImpact* **2017**, *6*, 39–54. [CrossRef]
75. Bai, W.; Raghavendra, A.; Podila, R.; Brown, J.M. Defect density in multiwalled carbon nanotubes influences ovalbumin adsorption and promotes macrophage activation and CD4+ T-cell proliferation. *Int. J. Nanomed.* **2016**, *11*, 4357–4371. [CrossRef]
76. Siegrist, K.J.; Reynolds, S.H.; Porter, D.W.; Mercer, R.R.; Bauer, A.K.; Lowry, D.; Cena, L.; Stueckle, T.A.; Kashon, M.L.; Wiley, J.; et al. Mitsui-7, heat-treated, and nitrogen-doped multi-walled carbon nanotubes elicit genotoxicity in human lung epithelial cells. *Part. Fibre Toxicol.* **2019**, *16*, 1–19. [CrossRef] [PubMed]
77. Kuku, G.; Saricam, M.; Akhatova, F.; Danilushkina, A.; Fakhrullin, R.; Culha, M. Surface-Enhanced Raman Scattering to Evaluate Nanomaterial Cytotoxicity on Living Cells. *Anal. Chem.* **2016**, *88*, 9813–9820. [CrossRef]
78. Sanpui, P.; Zheng, X.; Loeb, J.C.; Bisesi, J.H.; Khan, I.A.; Afrooz, N.R.M.N.; Liu, K.; Badireddy, R.R.; Wiesner, M.R.; Ferguson, P.L.; et al. Single-walled carbon nanotubes increase pandemic influenza A H1N1 virus infectivity of lung epithelial cells. *Part. Fibre Toxicol.* **2014**, *11*, 1–15. [CrossRef] [PubMed]
79. Rozhina, E.; Batasheva, S.; Miftakhova, R.; Yan, X.; Vikulina, A.; Volodkin, D.; Fakhrullin, R. Comparative cytotoxicity of kaolinite, halloysite, multiwalled carbon nanotubes and graphene oxide. *Appl. Clay Sci.* **2021**, *205*, 106041. [CrossRef]
80. Mishra, A.; Stueckle, T.A.; Mercer, R.R.; Derk, R.; Rojanasaku, Y.; Castranova, V.; Wang, L. Identification of TGF-β receptor-1 as a key regulator of carbon nanotube-induced fibrogenesis. *Am. J. Physiol.-Lung Cell. Mol. Physiol.* **2015**, *309*, L821–L833. [CrossRef]
81. Marangon, I.; Boggetto, N.; Ménard-Moyon, C.; Venturelli, E.; Béoutis, M.L.; Péchoux, C.; Luciani, N.; Wilhelm, C.; Bianco, A.; Gazeau, F. Intercellular carbon nanotube translocation assessed by flow cytometry imaging. *Nano Lett.* **2012**, *12*, 4830–4837. [CrossRef] [PubMed]
82. Sager, T.M.; Wolfarth, M.W.; Battelli, L.A.; Leonard, S.S.; Andrew, M.; Steinbach, T.; Endo, M.; Tsuruoka, S.; Porter, D.W.; Castranova, V. Investigation of the pulmonary bioactivity of double-walled carbon nanotubes. *J. Toxicol. Environ. Health-Part A Curr. Issues* **2013**, *76*, 922–936. [CrossRef]
83. Knudsen, K.B.; Berthing, T.; Jackson, P.; Poulsen, S.S.; Mortensen, A.; Jacobsen, N.R.; Skaug, V.; Szarek, J.; Hougaard, K.S.; Wolff, H.; et al. Physicochemical predictors of Multi-Walled Carbon Nanotube–induced pulmonary histopathology and toxicity one year after pulmonary deposition of 11 different Multi-Walled Carbon Nanotubes in mice. *Basic Clin. Pharmacol. Toxicol.* **2019**, *124*, 211–227. [CrossRef]
84. Lim, C.S.; Porter, D.W.; Orandle, M.S.; Green, B.J.; Barnes, M.A.; Croston, T.L.; Wolfarth, M.G.; Battelli, L.A.; Andrew, M.E.; Beezhold, D.H.; et al. Resolution of Pulmonary Inflammation Induced by Carbon Nanotubes and Fullerenes in Mice: Role of Macrophage Polarization. *Front. Immunol.* **2020**, *11*, 1–23. [CrossRef] [PubMed]
85. Khaliullin, T.O.; Shvedova, A.A.; Kisin, E.R.; Zalyalov, R.R.; Fatkhutdinova, L.M. Evaluation of Fibrogenic Potential of Industrial Multi-Walled Carbon Nanotubes in Acute Aspiration Experiment. *Bull. Exp. Biol. Med.* **2015**, *158*, 684–687. [CrossRef]
86. Porter, D.W.; Hubbs, A.F.; Chen, B.T.; McKinney, W.; Mercer, R.R.; Wolfarth, M.G.; Battelli, L.; Wu, N.; Sriram, K.; Leonard, S.; et al. Acute pulmonary dose-responses to inhaled multi-walled carbon nanotubes. *Nanotoxicology* **2013**, *7*, 1179–1194. [CrossRef]
87. Sager, T.M.; Wolfarth, M.W.; Andrew, M.; Hubbs, A.; Friend, S.; Chen, T.; Porter, D.W.; Wu, N.; Yang, F.; Hamilton, R.F.; et al. Effect of multi-walled carbon nanotube surface modification on bioactivity in the C57BL/6 mouse model. *Nanotoxicology* **2014**, *8*, 317–327. [CrossRef]
88. Holian, A.; Hamilton, R.F.; Wu, Z.; Deb, S.; Trout, K.L.; Wang, Z.; Bhargava, R.; Mitra, S. Lung deposition patterns of MWCNT vary with degree of carboxylation. *Nanotoxicology* **2019**, *13*, 143–159. [CrossRef] [PubMed]
89. Hamilton, R.F.; Wu, Z.; Mitra, S.; Holian, A. The effects of varying degree of MWCNT carboxylation on bioactivity in various in vivo and in vitro exposure models. *Int. J. Mol. Sci.* **2018**, *19*, 354. [CrossRef] [PubMed]
90. Kim, J.S.; Sung, J.H.; Song, K.S.; Lee, J.H.; Kim, S.M.; Lee, G.H.; Ahn, K.H.; Lee, J.S.; Shin, J.H.; Park, J.D.; et al. Persistent DNA Damage Measured by Comet Assay of Sprague Dawley Rat Lung Cells after Five Days of Inhalation Exposure and 1 Month Post-Exposure to Dispersed Multi-Wall Carbon Nanotubes (MWCNTs) Generated by New MWCNT Aerosol Generation System. *Toxicol. Sci.* **2012**, *128*, 439–448. [CrossRef]
91. Kim, J.S.; Sung, J.H.; Choi, B.G.; Ryu, H.Y.; Song, K.S.; Shin, J.H.; Lee, J.S.; Hwang, J.H.; Lee, J.H.; Lee, G.H.; et al. In vivo genotoxicity evaluation of lung cells from Fischer 344 rats following 28 days of inhalation exposure to MWCNTs, plus 28 days and 90 days post-exposure. *Inhal. Toxicol.* **2014**, *26*, 222–234. [CrossRef]
92. Smith, B.R.; Ghosn, E.E.B.; Rallapalli, H.; Prescher, J.A.; Larson, T.; Herzenberg, L.A.; Gambhir, S.S. Selective uptake of single-walled carbon nanotubes by circulating monocytes for enhanced tumour delivery. *Nat. Nanotechnol.* **2014**, *9*, 481–487. [CrossRef] [PubMed]
93. Mercer, R.R.; Hubbs, A.F.; Scabilloni, J.F.; Wang, L.; Battelli, L.A.; Friend, S.; Castranova, V.; Porter, D.W. Pulmonary fibrotic response to aspiration of multi-walled carbon nanotubes. *Part. Fibre Toxicol.* **2011**, *8*, 21. [CrossRef] [PubMed]
94. Mercer, R.R.; Scabilloni, J.F.; Hubbs, A.F.; Battelli, L.A.; McKinney, W.; Friend, S.; Wolfarth, M.G.; Andrew, M.; Castranova, V.; Porter, D.W. Distribution and fibrotic response following inhalation exposure to multi-walled carbon nanotubes. *Part. Fibre Toxicol.* **2013**, *10*, 33. [CrossRef]

95. Stapleton, P.A.; Minarchick, V.C.; Cumpston, A.M.; McKinney, W.; Chen, B.T.; Sager, T.M.; Frazer, D.G.; Mercer, R.R.; Scabilloni, J.; Andrew, M.E.; et al. Impairment of coronary arteriolar endothelium-dependent dilation after multi-walled carbon nanotube inhalation: A time-course study. *Int. J. Mol. Sci.* **2012**, *13*, 13781–13803. [CrossRef]
96. Mercer, R.R.; Scabilloni, J.F.; Hubbs, A.F.; Wang, L.; Battelli, L.A.; McKinney, W.; Castranova, V.; Porter, D.W. Extrapulmonary transport of MWCNT following inhalation exposure. *Part. Fibre Toxicol.* **2013**, *10*, 1. [CrossRef] [PubMed]
97. Di, Y.P.; Tkach, A.V.; Yanamala, N.; Stanley, S.; Gao, S.; Shurin, M.R.; Kisin, E.R.; Kagan, V.E.; Shvedova, A. Dual acute proinflammatory and antifibrotic pulmonary effects of short palate, lung, and nasal epithelium clone-1 after exposure to carbon nanotubes. *Am. J. Respir. Cell Mol. Biol.* **2013**, *49*, 759–767. [CrossRef] [PubMed]
98. Kagan, V.E.; Kapralov, A.A.; St. Croix, C.M.; Watkins, S.C.; Kisin, E.R.; Kotchey, G.P.; Balasubramanian, K.; Vlasova, I.I.; Yu, J.; Kim, K.; et al. Lung macrophages Digest carbon nanotubes using a superoxide/peroxynitrite oxidative pathway. *ACS Nano* **2014**, *8*, 5610–5621. [CrossRef] [PubMed]